Materials Horizons

ROYAL SOCIETY OF CHEMISTRY

COMMUNICATION

View Article Online
View Journal | View Issue

Cite this: *Mater. Horiz.*, 2026, 13, 3853

Received 5th December 2025,
Accepted 30th January 2026

DOI: 10.1039/d5mh02330k

rsc.li/materials-horizons

Cu_2ZnSnS_4–*Sporomusa ovata* photobiohybrids coupled with *Clostridium kluyveri* fermentation for CO_2 conversion to C_4–C_6 fatty acids

Muhammed Rishan,[ab] Prabeesh Punathil,[c] Cathal Burns,[ab] Elisabetta Arca,[d] Julio do Nascimento,[e] Vlado K. Lazarov,[ef] Guillaume Zoppi,[c] Martin Hayes,[g] Elizabeth A. Gibson[b] and Shafeer Kalathil *[a]

The conversion of greenhouse CO_2 into long-chain chemicals remains a major challenge in artificial photosynthesis. Here, we present a novel semi-biological platform that integrates microbial photocatalysis with fermentation to produce fatty acids from CO_2. The process begins with light-driven CO_2 reduction to acetate and ethanol, enabled by a photobiohybrid composed of the earth-abundant, non-toxic semiconductor Cu_2ZnSnS_4 (CZTS) and the CO_2-fixing electrotroph *Sporomusa ovata (S. ovata)*. In this CZTS–*S. ovata* hybrid, the CZTS nanoparticles act as light absorbers, generating reducing equivalents (electrons/H_2) that drive microbial CO_2 conversion. Under continuous illumination for five days, the system exhibited excellent biocompatibility and reusability, yielding acetate (1.035 ± 0.05 mmol g^{-1}) and ethanol (0.967 ± 0.04 mmol g^{-1}). These C_2 intermediates were subsequently upgraded *via* microbial chain elongation by *Clostridium kluyveri* (*C. kluyveri*), producing C_4 butyric acid (2.78 ± 0.2 μmol), C_6 caproic acid (1.08 ± 0.3 μmol), and H_2 (2.4 ± 0.4 μmol). This integrated photocatalysis–fermentation strategy showcases a sustainable route for solar-to-chemical energy conversion, offering a promising solution for carbon valorisation through the convergence of materials science and biotechnology.

New concepts

Overcoming the kinetic and thermodynamic limitations of C–C bond formation remains a major challenge in artificial photosynthesis. Here, we present a modular photobiohybrid system that integrates the earth-abundant quaternary chalcogenide semiconductor Cu_2ZnSnS_4 with the CO_2-fixing bacterium *Sporomusa ovata* for light-driven conversion of CO_2 into multicarbon products. This hybrid interface enables selective and stable photocatalytic reduction of CO_2 to acetate and ethanol under ambient conditions, leveraging the complementary advantages of inorganic light absorption and microbial specificity. Importantly, these C_2 products are further upgraded *via* microbial chain elongation to generate C_4 (butyric acid) and C_6 (caproic acid) fatty acids, demonstrating a two-stage carbon valorisation pathway. This work showcases a scalable, materials-integrated platform for solar-to-chemical energy conversion, offering new opportunities for sustainable carbon capture and utilisation using abundant elements and biologically tunable specificity.

Introduction

Amid the escalating global energy crisis and CO_2-driven climate change, there is an urgent need for renewable energy solutions, particularly those harnessing solar energy through carbon capture and utilisation (CCU) technologies.[1] Inspired by natural photosynthesis, various methods for solar-powered fuel and chemical production have been explored *via* artificial photosynthesis, which looks to mimic nature with synthetic materials. These approaches include photovoltaic-powered electrolysis,[2] photoelectrochemical systems,[3] and photocatalytic water splitting/CO_2 reduction.[4,5] These artificial systems aim to mimic natural photosynthesis by utilizing light-absorbing semiconductors that transfer energy to co-catalysts, to drive thermodynamically challenging reactions to generate storable fuels and chemicals.[6] However, the products generated by these systems are primarily limited to single-carbon (C_1) molecules, such as CO and HCOOH.[7,8] Furthermore, challenges related to efficiency, long-term stability, and high investment costs continue to impede the advancement and widespread adoption of these technologies.[9,10] To address these challenges, semi-biological photosynthetic systems offer a hybrid approach that combines light-absorbing materials with biocatalysts, creating a promising platform for the sustainable production of chemicals and fuels from CO_2 and sunlight.[11] These systems can

[a] *Faculty of Science and Environment, School of Geography and Natural Sciences, Northumbria University, Newcastle upon Tyne NE1 8ST, UK. E-mail: shafeer.kalathil@northumbria.ac.uk*
[b] *School of Natural and Environmental Sciences, Newcastle University, Newcastle upon Tyne NE1 7RU, UK*
[c] *Faculty of Science and Environment, School of Engineering, Physics and Mathematics, Northumbria University, Newcastle upon Tyne NE1 8ST, UK*
[d] *School of Mathematics, Statistics and Physics, Newcastle University, Newcastle upon Tyne NE1 7RU, UK*
[e] *School of Physics, Engineering and Technology, University of York, Heslington, UK*
[f] *York JEOL Nanocentre, Helix House, Science Park, University of York, Heslington, York, UK*
[g] *Johnson Matthey Technology Centre, Cambridge Science Park, Milton Road, Cambridge CB4 0FP, UK*

utilize either enzymatic or whole-cell strategies (microbes), where the bio-components typically function as catalysts to drive endergonic and complex chemical reactions. The light-absorbing material serves as a scaffold to immobilize the biocatalysts, facilitate charge transfer, and enable product separation.[12] Compared to enzyme-based biohybrids, the whole-cell approach offers several advantages, including stability, self-replication, self-repair, and adaptability to environmental perturbations such as changes in pH, temperature, and nutrient availability.[13,14] Additionally, the whole-cell catalysis operates in a cascade fashion, with multiple metabolic pathways and enzymes working continuously and selectively to generate $C_{2/2+}$ chemicals from CO_2.[11]

Autotrophic, non-photosynthetic CO_2-fixing microbes possess metabolic pathways that allow them to convert CO_2 into higher-value chemicals with remarkable selectivity and stability, even under environmental stress.[15] By hybridizing these microbes with light-absorbing or electron donating surfaces, chemolithoautotrophic growth can be achieved, facilitating the conversion of CO_2 into valuable chemicals.[16] This approach has been explored by integrating various inorganic and to a lesser extent, organic light-absorbing materials with microbes.[17,18] The first whole-cell inorganic biohybrid was demonstrated by Honda *et al.* where they integrated a recombinant strain of *E. coli* with TiO_2 nanoparticles for photocatalytic H_2 production using methyl viologen (MV^{2+}) as an electron mediator.[19] Several subsequent studies have explored the integration of inorganic semiconductors with CO_2 reducing microbes, majorly Cd based materials with acetogenic microbes for solar acetate producitons.[19–22] However, these systems have generally exhibited limited operational stability and a narrow product scope, typically terminating at acetate as the dominant reduction product. In addition to their cytotoxic nature, Cd-based semiconductors possess relatively wide bandgaps (*e.g.*, ~2.4 eV for CdS), restricting solar absorption to the blue-green region and leaving much of the visible spectrum unused. These limitations translate directly into reduced photocarrier generation and diminished driving force for deeper CO_2 reduction reactions in whole-cell biohybrids. Together with toxicity concerns that compromise microbial viability and scalability,[23] these optical constraints underscore the need for Cd-free, earth-abundant materials capable of harvesting a broader portion of the solar spectrum, criteria that motivate the introduction of CZTS-based biohybrids in the present study.

In this work, we present a biohybrid system that integrates the earth-abundant, cost-effective, non-toxic metal chalcogenide light-absorber CZTS nanoparticles with the CO_2-utilizing, non-photosynthetic bacterium *S. ovata*. Under solar irradiation, this biohybrid system efficiently reduces CO_2, resulting in the production of acetate and ethanol. In an innovative step, we further enhanced the value of these products by converting them into medium-chain fatty acids through fermentation. For this conversion, we utilized *C. kluyveri*, a bacterium capable of chain elongation using acetate and ethanol as feedstocks, which successfully produced butyrate, caproate, and H_2 as a byproduct. Our results establish a proof-of-concept for a microbial strategy in carbon utilisation, demonstrating the conversion of CO_2 into valuable medium-chain fatty acids and offering a promising route for sustainable carbon capture and transformation. To our knowledge, this work represents the first demonstration of a fully Cd-free semiconductor–*S. ovata* biohybrid that not only sustains phototrophic CO_2 fixation, but also enables light-driven downstream biological upgrading to C_4–C_6 products.

Results and discussion

Synthesis and characterization of CZTS nanoparticles

Building on our expertise with CZTS nanoparticle inks as absorber layers in thin-film photovoltaics, the material was synthesized *via* a well-established hot-injection method.[24] Following synthesis, the nanoparticles were thoroughly washed and size-profiled according to standard protocols.[25] Fourier transform-infrared (FT-IR) spectroscopy analysis of the washed particles showed the removal of most loosely bound oleylamine ligands (Fig. S1, SI), with only a small fraction of strongly coordinated amines remaining on the surface. This residual ligand population is expected to contribute to colloidal stability in aqueous media without impeding catalytic activity or microbial interfacing. Special attention was given to minimizing particle size with each successive wash. Particle size is a critical factor in this context, as both the exciton lifetime and its propagation to the solution interface are highly dependent on size.[26] Furthermore, our primary objective was to integrate the light-absorbing units onto the microbial surface. To facilitate effective integration, the CZTS particles had to be significantly smaller than the bacterial cells, ensuring optimal interaction and attachment.

The optical absorption behaviour is a key factor influencing the photocatalytic activity of a material. The UV-vis absorbance of the CZTS nanoparticles was analysed both as a film and in a toluene solution (Fig. 1a). Consistent with previous studies, the sample exhibited broad absorption spanning from the UV to visible region, with a noticeable absorption onset around 650 nm.[27] Tauc plot was used to determine the optical bandgap of the material, which was found to be 1.73 eV, indicating its suitability for visible light absorption (inset of Fig. 1a). The crystalline structure of the CZTS nanoparticles was examined by XRD (Fig. 1b), where the major diffraction peaks at 28°, 47°, and 56° correspond to the (112), (220), and (312) planes of the kesterite CZTS.[28]

The morphology and composition of the CZTS nanocrystals were characterized using SEM and TEM analyses. As shown in Fig. 2, TEM imaging revealed monodisperse nanoparticles with diameters ranging from 4 to 18 nm, with an average diameter of ~11.3 nm (Fig. S2, SI). The corresponding SAED pattern exhibited well-defined diffraction rings that index to the characteristic (*hkl*) planes of the kesterite CZTS structure, consistent with the XRD results. High-resolution TEM and STEM images further showed clear lattice fringes and the atomic columns of CZTS nanoparticles, indicating a high degree of crystallinity.

Elemental distribution evaluated using STEM-EDS mapping demonstrated uniform spatial dispersion of Cu, Zn, Sn, and

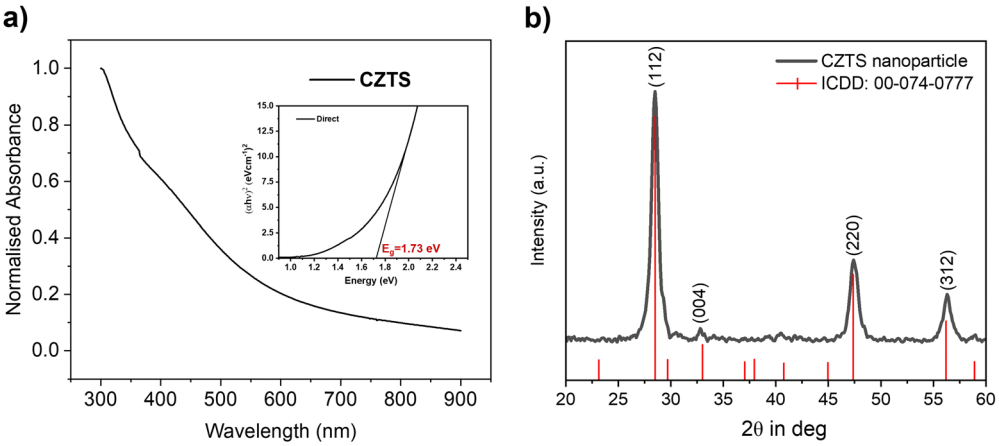

Fig. 1 Characterization of CZTS nanoparticles. (a) UV-Visible absorbance spectrum of the as-synthesized CZTS nanoparticles. Inset: Tauc plot used to determine the band gap of the material. (b) XRD pattern of the CZTS nanoparticles, with peaks at 2θ values of 28.53°, 47.33°, and 56.17°, corresponding to the d_{112}, d_{220}, and d_{312} phases of kesterite CZTS.

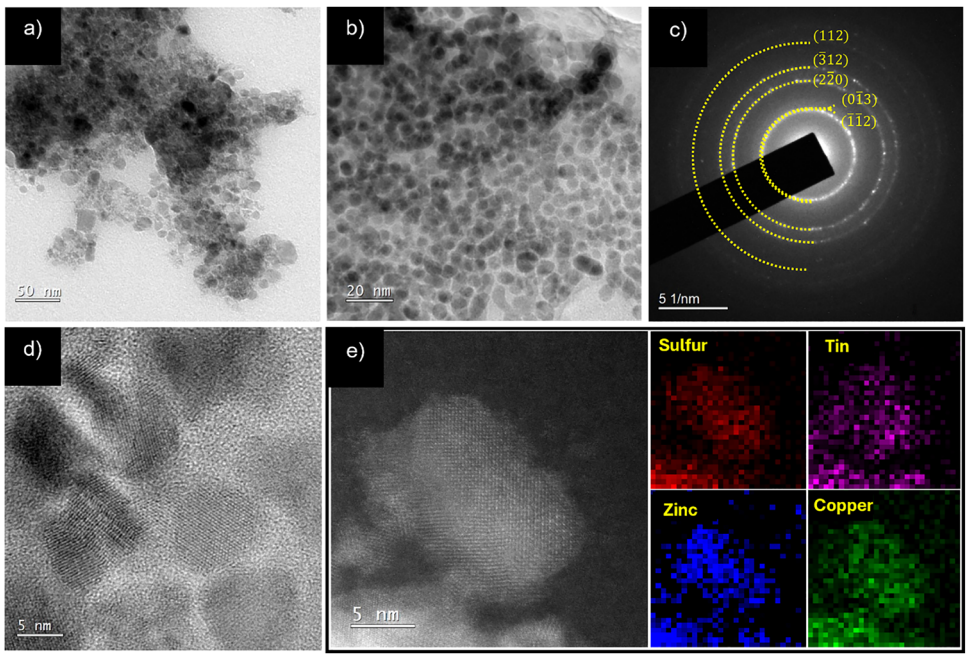

Fig. 2 Transmission electron microscopy (TEM) characterization of the CZTS nanoparticles synthesized *via* hot-injection method. (a) Representative TEM image of the as-synthesized nanoparticles, (b) TEM images of CZTS particles post-photobiocatalysis, (c) selected area electron diffraction (SAED) pattern of as-synthesized nanoparticles (d) high resolution-TEM (HR-TEM) images of representative CZTS nanoparticles showing good crystallinity. (e) Scanning TEM (STEM) image and corresponding energy dispersive X-ray spectroscopy (EDS) elemental maps confirming the homogeneous spatial distribution of Cu, Zn, Sn, and S throughout the nanocrystals.

S within the nanoparticles (Fig. 2e and Fig. S3, SI), consistent with the elemental composition observed in the SEM-EDS spectrum (Fig. S4, SI). The elemental composition obtained from SEM-EDS corresponds to an approximate atomic ratio of Cu : Zn : Sn : S $\approx$ 1.8 : 1.2 : 1 : 3.5, characteristic of a slightly Cu-poor and Zn-rich kesterite phase. This composition was further corroborated by inductively coupled plasma–optical emission spectroscopy (ICP–OES) of the nitric acid-digested particles (for Cu, Zn, Sn) and combustion based CHNS analysis (for S), which yielded closely matching elemental ratios with SEM-EDS data (Table S1, SI).

XPS analysis confirmed the valence states and purity of the elements on the surface of the CZTS nanoparticles (Fig. 3). Survey spectra were acquired confirming the purity of the material with all the main elements – Cu, Zn, S and Sn present (Fig. S5, SI). The only contaminants were oxygen, carbon and nitrogen, which are unavoidable for samples exposed to air. Aside from minor of surface oxidation (Fig. S6, SI), all peaks are attributed to the CZTS phase with the characteristic binding energy separation between the metal peaks (Zn, Cu, and Sn) and the S atom as previously reported in literature.[29–32]

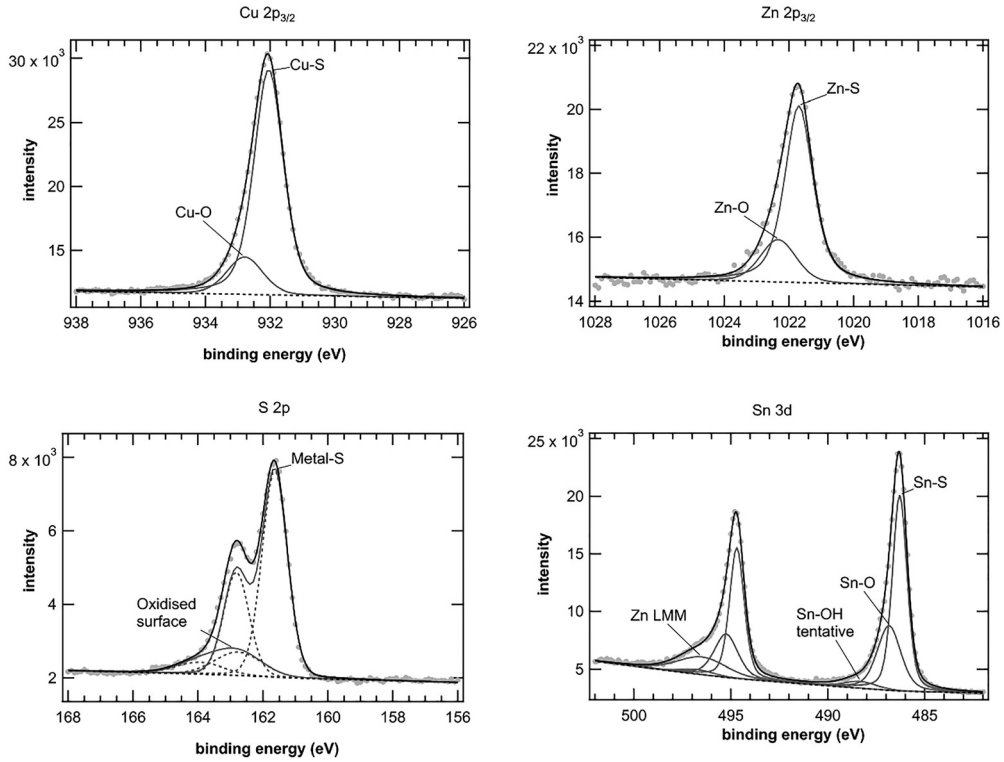

Fig. 3 X-ray photoelectron spectroscopy (XPS) analysis of CZTS. High-resolution XPS spectra of Cu (2p), Zn (2p), S (2p) and Sn (3d) in the CZTS nanoparticles.

As shown in Fig. 3, the Cu (2p) spectrum displayed the expected spin–orbit splitting with narrow peaks at 931.9 and 951.8 eV, and the expected spin–orbit separation of 19.8 eV.[33] Since the two components are well separated, the analysis has been focused on the Cu $2p_{3/2}$ and the peak shows predominantly a Cu–S environment, with only trace amounts of surface oxidation. A similar situation is observed for the Zn (2p) spectrum, which exhibited the spin–orbit components at 1021.7 and 1044.8 eV, with a separation of 23.1 eV, very close to the expected value of 23.0 eV.[24] Similarly to Cu, the spin orbit components are well separated and only the Zn $2p_{3/2}$ is used for the chemical state analysis. Similarly, to the Cu, the main component is a Zn–S bond, with only trace amount of oxidation. The Sn 3d region is slightly more complex, as it is superimposed to the Zn LMM Auger lines. The main chemical environment is still a Sn–S component, with spin orbit splitting as expected at 8.4 eV and the typical binding energy separation between the Sn $3d_{5/2}$ line and the S $2p_{3/2}$ characteristic of CZTS. Two more chemical environments are visible on the higher binding energy side of the spectrum, which have been attributed to surface oxidation. The S region display the characteristic doublet ($2p_{3/2}$ and $2p_{1/2}$) with the characteristic binding energy separation of 1.18 eV.[34] The main component is attributed to S in the CZTS compound, with the smaller component attributed to some surface oxidation. In conclusion the analysis of the XPS spectra confirm the purity of the CZTS phase with only trace amount of surface oxidation as a result of the fact that samples were handled in air. Together, these results verify that the hot-injection synthesis method reliably produces phase-pure, compositionally homogeneous CZTS nanocrystals without detectable secondary phases.

Before conducting photo-biocatalysis with *S. ovata*, the light-responsive properties of the material deposited on conductive glass were first evaluated using photoelectrochemical (PEC) characterization. The CZTS film exhibited a photocurrent response of -5 μA cm^{-2} when a potential of -0.25 V *vs.* Ag/AgCl (0.5 M K_2CO_3, pH 7.5, N_2 atmosphere) was applied (Fig. S7, SI). The stable photocurrent illustrates the efficient light absorption and charge separation property of the material. Also, it highlights the potential of using CZTS-based photocathodes in conjunction with bacteria for microbial photoelectrosynthesis, as this would avoid the need for a sacrificial electron donor (SED) and instead perform water oxidation at a photoanode.

Assembly of CZTS–*Sporomusa ovata* biohybrid system

Previous studies have demonstrated the impressive activity and operational stability of CZTS in both suspension photocatalysis and photoelectrochemical cells for hydrogen evolution (HER) and CO_2 reduction reactions (CO_2RR).[35–39] Collectively, these works established CZTS as a promising sunlight harvester owing to its strong visible-light absorption, benign elemental composition, and compatibility with scalable solution-phase processing. However, despite these advantages, reported CZTS systems have typically relied on noble metal or molecular cocatalysts to achieve appreciable CO_2 conversion and have remained limited to simple two-electron products such as CO

and formate. A notable effort toward bio-integration combining multiple semiconductor quantum dots, including CZTS, with two microbial strains to enable whole cell enzymatic CO_2 conversion.[40] Yet, in that study, pairing CZTS with *Cupriavidus necator*, a CO_2-utilizing bacterium capable of producing polyhydroxybutyrate, yielded modest activity, attributed to an unfavourable alignment between the semiconductor redox levels and key intracellular enzymes.

Building on this foundation, the present work demonstrates a step-change in capability by showing that CZTS can be interfaced directly with *S. ovata* to form a fully Cd-free biohybrid capable of accessing deeper CO_2 reduction chemistry. In striking contrast to the narrow product scope reported for *S. ovata* coupled with other inorganic semiconductors (Table S8, SI), the CZTS–/*S. ovata* hybrid achieves photocatalytic conversion of CO_2 to acetate and ethanol, indicating that the semiconductor generates sufficiently reducing photocarriers to drive downstream branches of the Wood–Ljungdahl pathway. Furthermore, by leveraging these native C_2 metabolites as substrates for fermentative chain elongation, the biohybrid platform mediates the sunlight-driven synthesis of multi-carbon C_4 (butyrate) and C_6 (caproate) fatty acids. This expanded product landscape establishes a new benchmark, demonstrating that an earth-abundant, non-toxic semiconductor can enable multi-electron, multi-carbon CO_2 upgrading *via* an inorganic–microbial interface, thereby overcoming the toxicity, spectral limitations, and restricted selectivity that define prior semiconductor/*S. ovata* systems.

In this work, *S. ovata* (Fig. S8, SI), an electrotrophic bacterium capable of converting CO_2 into acetate and ethanol using electrons or hydrogen derived from electrode surfaces or photocatalysts, was employed for the CO_2RR.[16,41] Previous studies have shown that *S. ovata* can directly uptake H_2 or electrons from electrode surfaces to perform CO_2RR, producing valuable chemicals *via* the acetyl-CoA intermediate through the Wood–Ljungdahl pathway (WLP).[42]

Photobiohybrid assembly

In a typical reaction setup, 10 mg of as-synthesized CZTS nanoparticles were suspended in 6 mL of *S. ovata* media (Table S3, SI) containing 100 mM triethanolamine (TEOA) as the sacrificial electron donor (SED). *S. ovata* cells were then introduced into the reaction vial to achieve a final optical density (OD_{600}) of 1.0. The ratios of CZTS nanoparticles, *S. ovata* cells, and TEOA were optimized through preliminary screening experiments (Fig. S9, SI). The reaction mixture was purged with a gas mixture of N_2 : CO_2 (80 : 20%) for 45 minutes before being exposed to light under a Newport Oriel 67005 solar simulator (300 W, 100 mW cm^{-2}, AM 1.5 G filter attachment, 1 sun). The choice of an N_2 : CO_2 gas mixture in an 80 : 20 (pH 7.5) ratio was made to simulate the conditions found in coal-fired power plants, which emit flue gases containing 3–13% CO_2 by volume.[43] Previous studies have shown that carbon capture and storage (CCS) plants often utilize mono- and triethanolamine-based solvents to efficiently absorb CO_2.[44] In this context, TEOA added to the reaction medium not only serves as a hole scavenger for CZTS but also facilitates the dissolution of purged CO_2. The captured CO_2, partially converted to HCO_3^-, is subsequently utilised by *S. ovata* in its metabolic pathways. The association between CZTS nanoparticles and *S. ovata* is best described as a non-covalent, surface-level attachment. The zeta potential measurement of *S. ovata* (-47.4 ± 6.2 mV) cells and CZTS nanoparticles (-34.7 ± 2.8 mV) carry net negative surface charges in the reaction medium, yet ionic species present in the reaction medium (K^+/Na^+/PO_4^-) partially screen these charges, enabling effective electrical double-layer compression and promoting particle–cell proximity. Such screening, together with nonspecific van der Waals interactions, facilitates nanoparticle adhesion to the cell envelope under illumination, an effect consistent with earlier reports on *S. ovata*–semiconductor biohybrids.[45,46]

Photobiocatalytic chemical production

The CZTS–*S. ovata* biohybrid system effectively catalysed CO_2 reduction reaction (CO_2RR), as confirmed by ^{1}H NMR analysis of a reaction aliquot collected after two days of photocatalysis (Fig. 5a and Fig. S10, SI). The NMR spectrum displayed characteristic signals corresponding to acetate (δ 1.9 ppm, singlet, 3H) and ethanol (δ 1.2 ppm, triplet, 3H), both of which are established metabolites produced and utilized by *S. ovata* during autotrophic growth.[47–49] On five days of uninterrupted light operation, the biohybrid showed an activity of 1.035 ± 0.05 mmol g^{-1} of acetate and 0.967 ± 0.04 mmol g^{-1} of ethanol production from CO_2 (Fig. 5b).

Sporomusa species are generally homoacetogenic, meaning they primarily produce acetic acid by metabolizing a variety of substrates, especially C_1 compounds like CO/CO_2 mixture with H_2, hydroxy fatty acids, betaine (used during cultivation).[50] *S. ovata* shares these metabolic traits, reducing CO_2 to acetic acid *via* WLP for energy conservation.[51] The WLP comprises two main branches catalysed by formate dehydrogenase (FDH) and carbon monoxide dehydrogenase (CODH), which contribute the methyl and carbonyl groups, respectively, to the formation of the acetyl-CoA intermediate.[52] Homoacetogenic species including *S. ovata* have previously been shown to produce ethanol as secondary metabolite under chemoautotrophic growth conditions.[41,53] As illustrated in Fig. 4b, ethanol formation by *S. ovata via* the WLP may proceed through two potential routes: (i) direct reduction of acetyl-CoA to ethanol *via* an acetaldehyde intermediate, catalysed by acetaldehyde dehydrogenase (AldDH), or (ii) re-assimilation of acetate, initially produced during primary metabolism, catalysed by aldehyde:-ferredoxin oxidoreductases (AOR).[54,55]

The band energies of the CZTS photocatalyst were obtained from X-ray photoelectron spectroscopy (XPS) valence-band measurements, with the absolute energy scale referenced to the Fermi level determined from the ultra-violet photoelectron spectroscopy (UPS) measured work function calibrated against a gold reference (Fig. 5c–e). After conversion of vacuum level energy to SHE scales at pH 7, the valence and conduction band positions were found to be +0.21 V and −1.44 V, respectively. The highly negative conduction band lies well above the reduction potentials relevant to *S. ovata*–mediated CO_2 conversion pathways

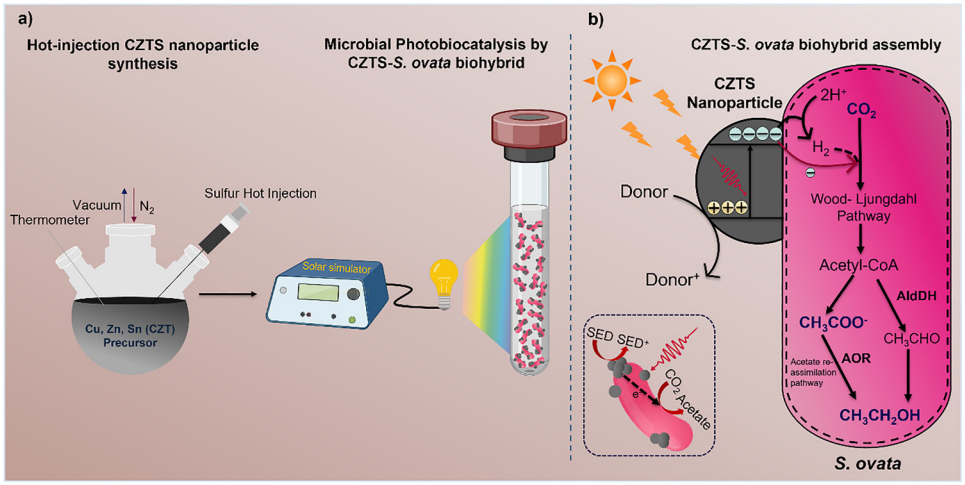

Fig. 4 Formation and reaction mechanism of the CZTS–*S. ovata* biohybrid system. (a) Schematic illustration of CZTS nanoparticle synthesis *via* hot-injection and their subsequent integration with *S. ovata* to form a photocatalytically active biohybrid. (b) Proposed mechanistic pathway for light-driven CO_2 conversion to acetate and ethanol by the CZTS–*S. ovata* hybrid. Under solar illumination, the CZTS nanoparticles generate excitons (electron–hole pairs), with photoexcited electrons promoted to the conduction band and transferred to *S. ovata*—either directly or through H_2 as an intermediate, to fuel CO_2 reduction *via* the acetyl-CoA (Wood–Ljungdahl) pathway. Simultaneously, photogenerated holes in the valence band are quenched by the sacrificial electron donor (SED), facilitating efficient charge separation and sustaining catalytic turnover. Inset: Conceptual depiction of light-driven CO_2 conversion to multicarbon products enabled by the CZTS–*S. ovata* biohybrid.

(H^+/H_2: −0.41 V; CO_2/CH_3CH_2OH: −0.33 V; CO_2/CH_3COOH: −0.27 V), thereby providing strong thermodynamic driving force for the photobiocatalytic reactions described in Fig. 4. At the same time, photogenerated holes in the valence band (+0.21 V) are effectively quenched by TEOA, whose oxidation potential (+0.18 V *vs.* SHE at pH 7) enables efficient hole scavenging and supports sustained charge separation under solar illumination.

Fundamentally, the mechanism of electron uptake by bacteria from donor surfaces during CO_2 reduction in microbial photobiocatalysis or electrosynthesis remains complex and not fully understood. Electron transfer can occur *via* two primary pathways: direct electron transfer (DET) or mediated electron transfer, where reducing equivalents such as H_2 or other redox mediators facilitate electron shuttling.[12] This ambiguity also applies to the present study, in which electron transfer from CZTS to *S. ovata* may proceed either directly or indirectly *via* H_2 mediation (Fig. 4b). Previous genomic analyses suggest that *S. ovata* encodes multiheme c-type cytochromes and hydrogenase enzymes,[56] which are commonly implicated in microbial extracellular electron transfer. If DET is operative in this system, it is likely facilitated by membrane-bound or extracellular hydrogenases and cytochromes. To probe the dominant electron transfer pathway, we quantified headspace H_2 levels generated during photobiocatalysis under standard reaction conditions and compared them with abiotic controls lacking bacteria (Fig. S11, SI). No significant difference in H_2 production was observed at any time point, suggesting that the majority of reducing equivalents utilized by *S. ovata* for CO_2 reduction are likely derived from direct electron transfer from photoexcited CZTS nanoparticles, rather than through H_2-mediated pathways. Although the conduction band minimum (CBM) of CZTS lies above the hydrogen evolution reaction (HER) potential (−0.42 V *vs.* SHE at pH 7),[57] hydrogen generation is expected to be kinetically limited in this system due to the absence of a HER co-catalyst (*e.g.*, Pd) on the CZTS surface.

SEM analysis of the biohybrid after three days of microbial photocatalysis revealed clear attachment of CZTS nanoparticles over bacterial cells (Fig. 6b–e). Elemental mapping *via* SEM–EDS confirmed the presence of carbon, consistent with microbial biomass associated within the biohybrid structure (Fig. 6f). Assessing the biocompatibility and potential cytotoxicity of semiconductor materials is critical for evaluating the stability and functionality of such biohybrid systems.[58] The long-term viability of *S. ovata* in the presence of CZTS was assessed using a LIVE/DEAD fluorescence assay (Fig. 7c). This assay employs two nucleic acid-binding dyes: SYTO 9, which stains all bacterial cells and emits green fluorescence, and propidium iodide (PI), which selectively penetrates only damaged or dead cells, emitting red fluorescence. Confocal laser scanning microscopy (CLSM) revealed predominantly green fluorescence, with minimal red signal (Fig. S12, SI), indicating a high proportion of viable, metabolically active cells even after 5 days of continuous photobiocatalysis in the presence of CZTS.

To further investigate the interaction between CZTS nanoparticles and *S. ovata* cells, the biohybrid suspension was analysed using Raman spectroscopy (Fig. 7a). Raman spectra of pristine CZTS, subjected to abiotic photocatalysis for 5 days in *S. ovata* growth medium containing a hole scavenger, exhibited two characteristic peaks at approximately 98 cm^{-1} and 350 cm^{-1}. These correspond to the E/B and A_1 symmetry vibrational modes of CZTS, respectively.[59,60] In contrast, the Raman spectrum of the CZTS–*S. ovata* biohybrid exhibited two additional broad bands alongside the characteristic vibrational modes of CZTS: one at ∼1500 cm^{-1} in the fingerprint region

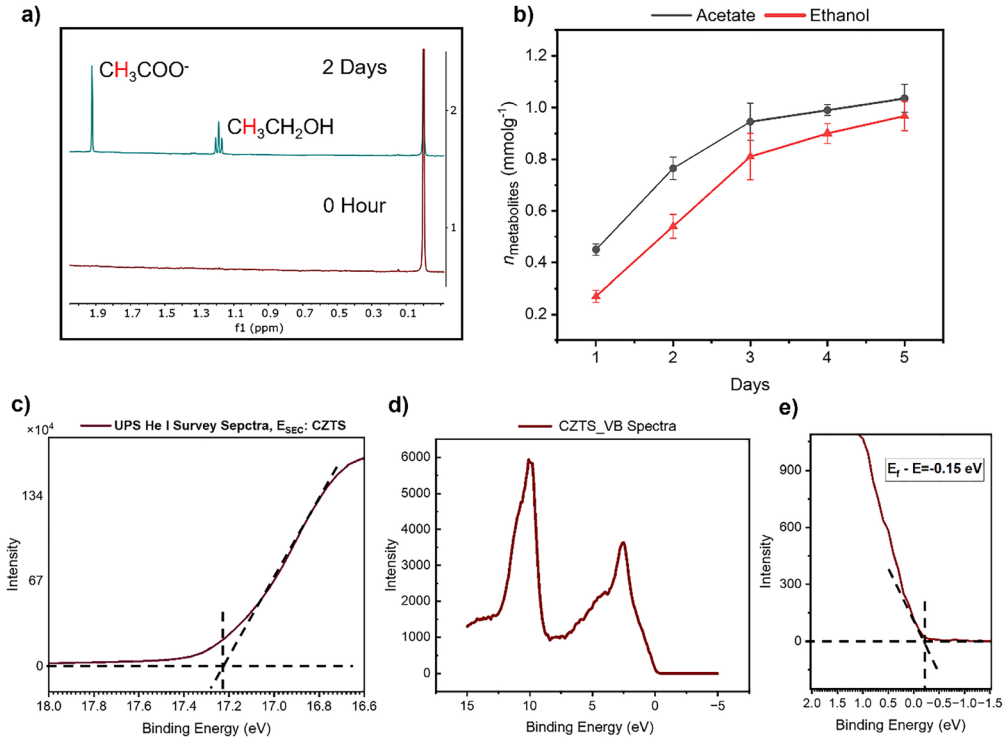

Fig. 5 Photobiocatalytic metabolite production by the CZTS–*S. ovata* biohybrid and photoelectron spectroscopy-based energy level analysis of CZTS. (a) Representative stacked ^{1}H NMR spectra (D_2O, 400 MHz) of the reaction medium collected before (0 hour) and after 2 days of photobiocatalysis. After 2 days, the spectrum shows characteristic peaks corresponding to acetate (δ 1.9 ppm, s, 3H) and ethanol (δ 1.2 ppm, t, 3H), indicating their production by the CZTS–*S. ovata* biohybrid during semi-biological photosynthesis. The reaction was carried out in a medium purged with an N_2 : CO_2 (80 : 20) gas mixture (pH 7.6), under ambient conditions (298 K, 1 atm) and 1 sun illumination (AM 1.5 G, 100 mW cm^{-2}). (b) Time-course production profiles of acetate and ethanol by the CZTS–*S. ovata* system. Error bars represent standard deviation (s.d) from triplicate experiments (n = 3). (c) Ultraviolet photoelectron spectroscopy (UPS) spectrum of CZTS, with the secondary electron cutoff region magnified to determine the work function (Φ). The Φ was calculated by subtracting the spectral width from the He I excitation energy (21.22 eV). (d) X-ray photoelectron spectra (XPS) VB full spectra. (e) Magnified XPS of the CZTS determining the VB level of the CZTS. Black dashed lines are the linear fits.

and another near 3000 cm^{-1} in the high wavenumber region. These peaks are attributed to vibrational modes of biomolecules, specifically proteins, lipids, and nucleic acids indicating the presence of microbial biomass on the CZTS surface.[61] This observation aligns with the negative zeta potential measured for *S. ovata* (−47.4 ± 6.2 mV), which reflects the abundance of phosphate, carboxylate, and polysaccharide groups on its outer membrane—in line with previously reported microbial membrane characteristics.[62,63]

The reusability of the CZTS–*S. ovata* biohybrid system was evaluated by subjecting it to multiple consecutive reaction cycles, each lasting 5 days. For each new cycle, only the reaction medium containing the SED was refreshed, while the biohybrid was retained. As shown in Fig. 7b, a slight decline in photocatalytic activity was observed over successive runs, as indicated by the gradual reduction in metabolite concentration. After three consecutive photobiocatalytic cycles, the biohybrid maintained ≈88% of its original catalytic activity, highlighting its durable performance and suitability for repeated use under continuous operation. SEM imaging of the reused biohybrid after the third cycle (Fig. 7d) showed consistent bacterial attachment and distribution on the CZTS particles, similar to the morphology observed after the initial 3-days of photobiocatalysis (Fig. 6b–e), further supporting the structural integrity and robustness of the biohybrid system.

Isotopic labelling experiments using $^{13}CO_2/H^{13}CO_3^-$ confirmed the carbon origin of the photobiocatalytic products by CZTS–*S. ovata* biohybrid. ^{1}H NMR analysis of the reaction aliquot after 5 days of light reaction showed the formation of ^{13}C-acetate ($^{13}CH_3{}^{13}COO^-$), demonstrating that CO_2 was the sole carbon source (Fig. S13, SI). Notably, while the unlabelled system produced both acetate and ethanol, the $^{13}CO_2$ experiment yielded only acetate. This outcome is consistent with the redox-dependent metabolism of *S. ovata*, where low reducing power directs carbon flux through the phosphotransacetylase/acetate kinase (PTA/ACK) pathway to acetate, while ethanol formation requires the more reducing AOR/ADH branch.[16] These results indicate that ethanol detected in the unlabelled system likely arises from secondary reduction of acetate under higher electron availability, rather than from direct CO_2 fixation. The amount of $^{13}CH_3{}^{13}COO^-$ quantified was approximately half of $^{12}CH_3{}^{12}COO^-$ that obtained under $^{12}CO_2/H^{12}CO_3^-$ conditions. This reduction is consistent with isotope-dependent effects reported in microbial CO_2-fixation pathways, where the incorporation and propagation of heavier isotopes through metabolic networks can alter enzymatic rates due to kinetic isotope effects.[64,65]

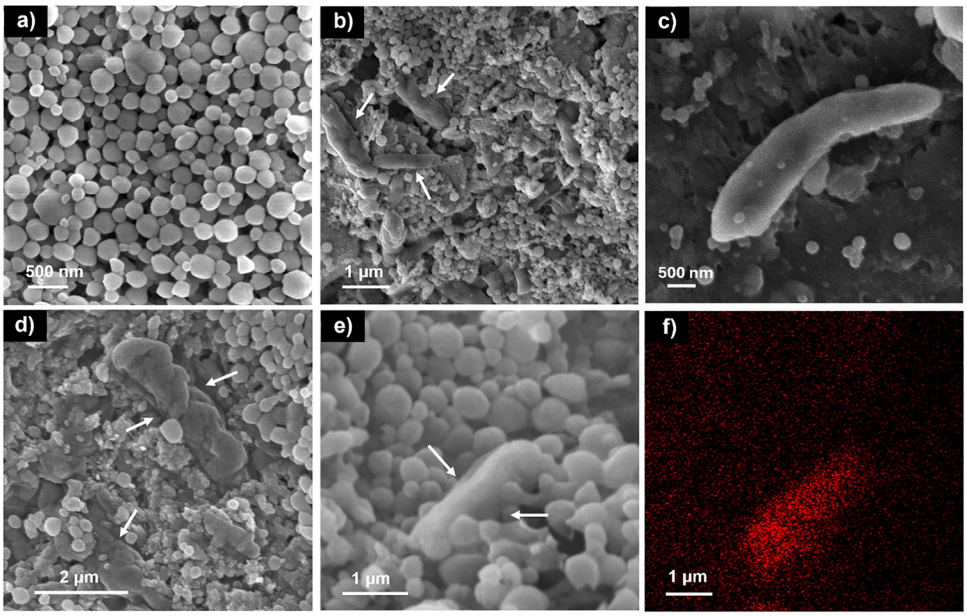

Fig. 6 Morphological characterization of the CZTS–*S. ovata* biohybrid system. (a) Scanning electron microscopy (SEM) images of the CZTS nanoparticles, (b)–(e) CZTS–*S. ovata* biohybrid after 3 days of photobiocatalysis, showing the interaction between CZTS nanoparticles and the bacterial surface. Arrows point to the biohybrid locations. Biohybrids in figure (c) and (d) shows the strong adhesion of CZTS nanoparticles on the cell membranes of *S. ovata*. (f) SEM-EDS mapping of carbon, confirming the spatial distribution of *S. ovata* biomass within the composite biohybrid structure.

To validate the role of each component in the photobiocatalytic system, a series of control experiments were performed by systematically omitting light, *S. ovata* cells, or CZTS nanoparticles from the reaction setup (Table S2, SI). None of the control conditions yielded acetate or ethanol at levels comparable to those observed under standard reaction conditions, thereby supporting the necessity of all components in the proposed mechanism. A trace amount of acetate (<0.1 mM) was detected in control trials that retained *S. ovata* cells but excluded other components. This minor acetate production is attributed to dark metabolism by *S. ovata*, utilizing residual internal carbon reserves accumulated during growth.[66] To further confirm that acetate and ethanol production arises specifically from the metabolic activity of *S. ovata*, an additional control was conducted using heat-killed (autoclaved) *S. ovata* cells. As expected, no metabolic products were detected in this condition, confirming that live, metabolically active cells are essential for the biocatalytic process.

TEM analysis of the CZTS nanoparticles after photobiocatalysis revealed a modest decrease in average particle size (from 11.33 nm to 6.54 nm, Fig. S2, SI), likely caused by mechanical shear and interparticle collisions during the extended stirring period in the photoreactor (5 days), which can induce minor fragmentation of colloidal nanocrystals. Importantly, complementary XRD and UV-vis measurements confirmed that no structural degradation or loss of crystallinity occurred (Fig. S14, SI), and the optical absorption onset of the particles remained unchanged after interaction with *S. ovata* and subsequent photo-experiments (Fig. S15, SI), indicating that the fundamental stability of the CZTS nanoparticles was preserved. Interestingly, an overall increase in absorption was observed in the CZTS–*S. ovata* biotic suspension relative to the abiotic control, which can be attributed to enhanced colloidal suspension stability induced by the bacterial cells that act as scaffolds to slow particle settling-enabling more active surface are to the light exposure. This improved dispersion likely contributes to the enhanced photobiocatalytic performance, consistent with the slightly higher HER activity observed in the CZTS–*S. ovata* heat-killed trials compared to abiotic controls (Fig. S11, SI).

To determine whether the CO_2 reduction products (acetate and ethanol) could act as hole scavenger to CZTS and potentially interfere with mechanistic interpretations, a control experiment was conducted under standard reaction conditions. In this setup, fresh CZTS was used, but TEOA was replaced with a mixture of acetate (1.8 mM) and ethanol (1.6 mM). After 5 days of illumination, no change in the concentrations of acetate or ethanol was observed, and no hydrogen or additional liquid-phase products were detected in the reaction medium. These results rule out the possibility of back reactions involving microbial metabolites acting as SEDs, supporting the integrity of the proposed mechanism. The pH of the reaction medium was continuously monitored using an *in situ* pH probe. Following purging with the $N_2:CO_2$ (80 : 20) gas mixture, the initial pH was recorded at 7.5. A gradual decrease in pH was observed over the course of the 5-day photobiocatalysis, reaching a final value of 6.6. This medium acidification consists of the formation of acidic metabolites and the oxidative degradation of TEOA. Importantly, the observed pH range remained well within the known physiological tolerance of *S. ovata* (pH 5.3–8.0) and far

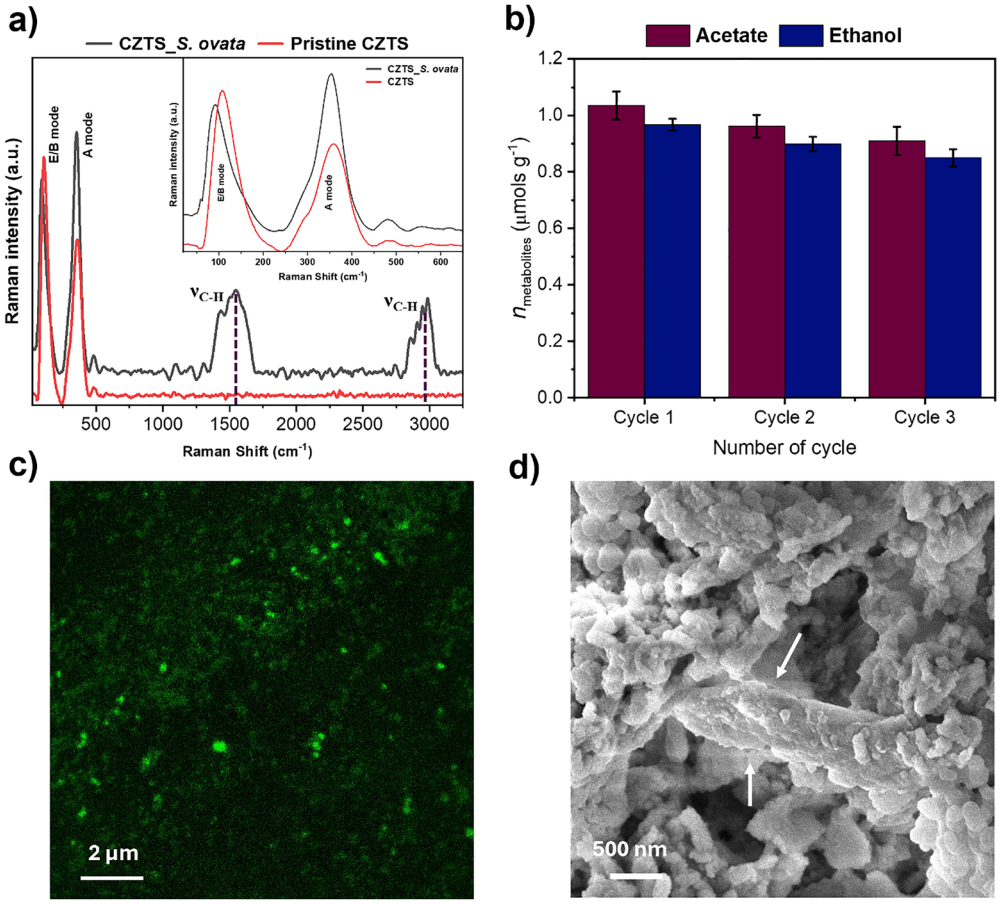

Fig. 7 Raman and viability study of the CZTS–*S. ovata* biohybrid. (a) Raman spectra of CZTS (abiotic, red) and CZTS_*S. ovata* (biotic, black) suspension analysed post photo experiment. Inset; Raman spectra of CZTS, intense peak around 350 cm^{-1} indicates the A_1 mode of the kesterite CZTS. The slight shift from standard value (340 cm^{-1}) can potentially be due to the sublattice disorder,[24] or minor photo degradation after 5 days of photobiocatalysis. (b) Reusability performance of the CZTS–*S. ovata* biohybrid system for acetate and ethanol production. The test was conducted over 3 cycles, each lasting 5 days, by reusing the biohybrid (*via* centrifugation). The reaction was carried out in a medium purged with an $N_2 : CO_2$ (80 : 20) gas mixture under ambient conditions (pH = 7.6, 298 K, 1 atm) with 1 sun illumination (AM 1.5 G, 100 mW cm^{-1}). Error bars represent s.d from triplicate experiments (n = 3). (c) Confocal laser scanning microscopy (CLSM) image showing live cells in the CZTS–*S. ovata* biohybrid after 5 days of microbial photobiocatalysis, stained with the live/dead bacterial viability kit. (d) SEM image of the CZTS–*S. ovata* biohybrid after 3 cycles of the reusability test. Arrows indicate the biohybrid structure.

from the acidity threshold at which enzymatic activity becomes compromised. Accordingly, no adverse effects on microbial metabolism or photobiocatalytic performance were expected or observed.[50]

Chain elongation of acetate and ethanol to fatty acids

Acetate and ethanol are widely utilized platform chemicals with broad applications in the polymer, textile, and biofuel industries.[67–69] Beyond their standalone value, these molecules serve as important precursors for the synthesis of higher-value products. One promising route involves upgrading acetate and ethanol into short-chain and medium-chain fatty acids (SCFAs and MCFAs), which possess 2–3 times greater energy density and are experiencing increasing commercial demand.[70–72] This transformation significantly enhances the utility and market potential of bio-based chemical platforms.

Here, we demonstrate the biological upgrading of solar-derived acetate and ethanol into medium-chain fatty acids *via* anaerobic fermentation, thereby directly linking photochemical CO_2 fixation with downstream microbial chain elongation (Fig. 8). The acetate and ethanol fermenting bacterium *C. kluyveri* (Fig. S16, SI) was employed for this purpose. By feeding *C. kluyveri* with acetate and ethanol produced from microbial photocatalysis using the CZTS–*S. ovata* biohybrid system, we achieved the successful production of butyrate (C_4) and caproate (C_6), with hydrogen as a metabolic byproduct. The chain elongation process in *C. kluyveri* proceeds through the well-characterized reverse β-oxidation pathway, wherein ethanol is sequentially added to butyrate, resulting in the formation of caproate and molecular H_2.[73] Both butyrate and caproate are valuable industrial chemicals with diverse applications, including in the manufacture of lubricants, antimicrobials, biodiesel ecursors, and animal feed additives.[74] Notably, caproate can be further upgraded into drop-in liquid fuels through catalytic processes such as ketonization and dehydrogenation, producing alkanes suitable for blending into

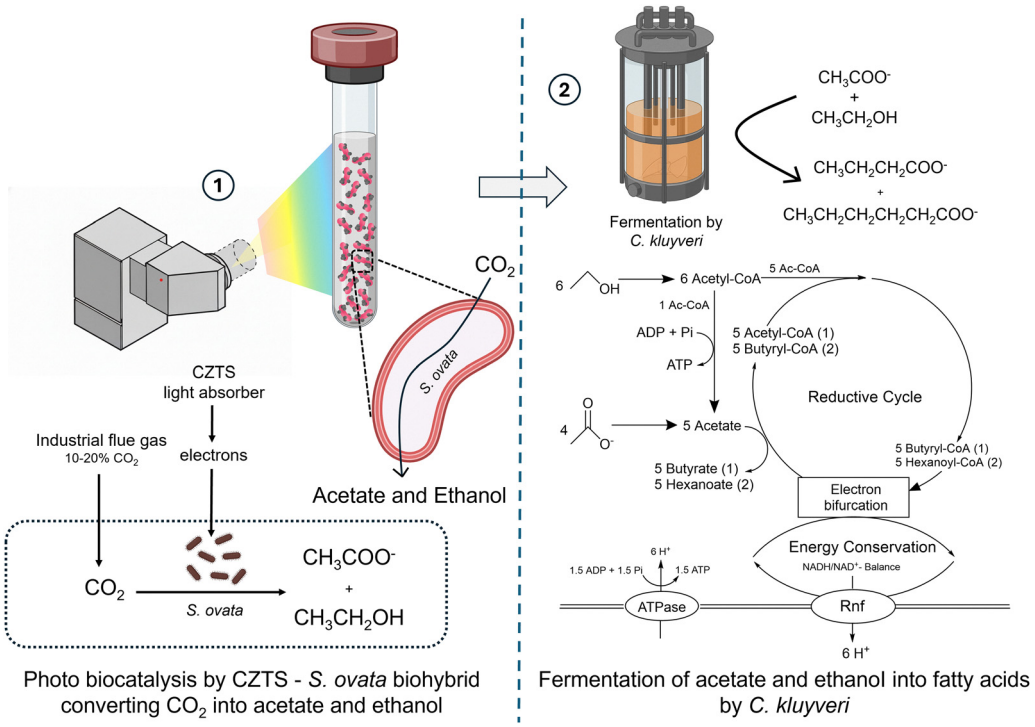

Fig. 8 Schematic representation of photobiocatalytic chemical production coupled with microbial fermentation. The integrated process is divided into two key stages: (1) solar irradiation of a photo biocatalytic setup comprising CZTS–*S. ovata* biohybrid, insets: a zoomed in version of *S. ovata* performing CO_2 reduction into acetate and ethanol. (2) The acetate and ethanol produced are subsequently upgraded to medium-chain fatty acids, butyrate (C_4) and caproate (C_6) *via* fermentation by *C. kluyveri*, operating through the reverse β-oxidation pathway.

biodiesel. Moreover, caproate is being explored as a promising precursor for the production of sustainable aviation fuels.[75]

$$6CH_3CH_2OH + 3CH_3COO^- \rightarrow 3CH_3CH_2CH_2COO^- + 1CH_3CH_2CH_2CH_2CH_2COO^- + 2H_2 + H^+ + 4H_2O \quad (1)$$

The fermentation process using *C. kluyveri* was carried out in a separate anaerobic compartment. The reaction medium from the photobiocatalysis step, filtered to remove biomass contained acetate (10.35 ± 0.5 μmol) and ethanol (9.67 ± 0.6 μmol s) which is used as the substrate for fermentation. *C. kluyveri* was cultured in DSMZ 556 medium (Table S4, SI) and maintained under strictly anoxic conditions by purging the headspace with an $N_2:CO_2$ (80:20) gas mixture. Although *C. kluyveri* does not require CO_2 for its metabolic activity, the $N_2:CO_2$ gas composition was intentionally maintained to mirror the conditions used in the preceding *S. ovata* photobiocatalytic step, ensuring consistency across both stages of the process and enabling a unified, reproducible operational environment.

The metabolic progression of *C. kluyveri* was monitored periodically using ^{1}H NMR spectroscopy of aliquots withdrawn from the fermentation vials. After 7 days of incubation, the formation of butyrate was confirmed by the appearance of characteristic peaks at δ 0.88 ppm (t, 3H), δ 1.54 ppm (m, 2H), and δ 2.14 ppm (t, 2H) (Fig. 9). By day 10, caproate production was also detected, marked by an isolated resonance at δ 1.34 ppm (m, 2H). Two additional characteristic peaks of caproate at δ 0.86 ppm (t, 3H) and δ 1.54 ppm (m, 2H) overlapped with the butyrate signals due to their similar aliphatic environments, making spectral deconvolution necessary for precise quantification. As typically observed in *C. kluyveri* driven fermentation, gas chromatography analysis of the headspace confirmed substantial H_2 production (Fig. S17, SI), supporting the expected metabolic activity associated with chain elongation *via* reverse β-oxidation.

The efficiency of fermentative product formation was calculated based on the stoichiometry of the standard chemical equations governing the chain elongation process (eqn (1)). Detailed quantification of the substrates and products is provided in Fig. 10. After 10 days of incubation, most of the ethanol supplied to *C. kluyveri* was consumed, while a trace level of acetate remained. This observation suggests that ethanol serves as the limiting reagent and is essential for driving the reverse β-oxidation pathway, in which it is sequentially elongated with acetate to form butyrate and subsequently caproate.[74] Fermentation efficiency was calculated relative to ethanol consumption. By day 10, the system had achieved 58 ± 4.7% of the theoretical yield for butyrate, 67.5 ± 19.3% for caproate, and 75 ± 13.1% for hydrogen. The deviation from theoretical yields likely reflects partial utilization of substrates for microbial maintenance and biomass growth, as well as potential kinetic limitations within the enzymatic steps of the chain elongation pathway. The carbon mass balance for the chain-elongation

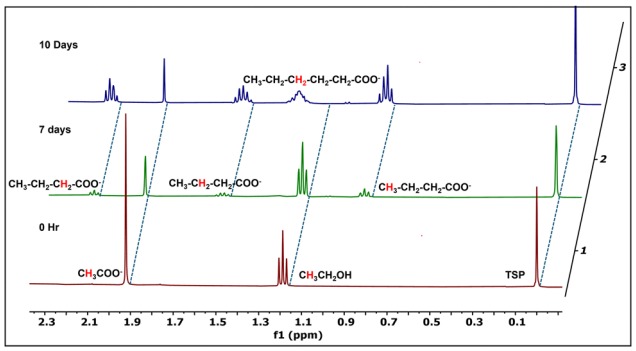

Fig. 9 Metabolic progress by *C. kluyveri* during fermentative chain elongation. ^{1}H NMR spectra of fermentation products by *C. kluyveri*. The TSP signal is set to 0 ppm in each spectrum. The stacked spectra are vertically and horizontally offset for clarity, as indicated by the blue dashed line.

step showed a total carbon input of 40.8 μmol (from 10.8 μmol acetate and 9.6 μmol ethanol), of which 19.0 μmol–corresponding to ∼47% recovery was accounted for in extracellular products (butyrate: 2.784 μmol; caproate: 1.08 μmol) and residual substrates (acetate: 0.55 μmol; ethanol: 0.15 μmol). The unrecovered fraction is attributed to intracellular metabolite accumulation (*e.g.*, acetyl-CoA intermediates), biomass formation, and CO_2 release inherent to reverse β-oxidation pathways, consistent with the established physiological behaviour of *C. kluyveri*.[76] Control experiments performed under a pure N_2 atmosphere showed that *C. kluyveri* maintained normal fermentative activity, demonstrating that CO_2 is not required for its metabolism, in agreement with previous reports.[74] The carbon mass balance calculation of the fermentative chain elongation revealed a total carbon recovery around 50%, remaining fraction to be contributed for intracellular metabolite accumulation, biomass formation and CO_2 evolution during reverse β-oxidation. Additionally, a control experiment was conducted using TEOA and its oxidized derivatives under standard fermentation conditions. No fermentation products were detected after 10 days, confirming that *C. kluyveri* does not metabolize TEOA or its oxidation products.

Conclusion

In conclusion, this study establishes a novel two-step strategy for the conversion of CO_2 into high-value SC/MCFA by integrating semi-biological photosynthesis with fermentative chain elongation. We assembled a photocatalytic biohybrid system integrating nanocomposite CZTS particles with CO_2 fixing *S. ovata*. The CZTS–*S. ovata* biohybrid performed CO_2 reduction, producing acetate and ethanol under sacrificial conditions where TEOA served as the SED quenching photogenerated holes in CZTS. Followed by this, the acetate and ethanol produced were taken for fermentative chain elongation in a different compartment catalysed by *C. kluyveri*, producing butyrate, caproate and H_2. The CZTS has shown remarkable stability and biocompatibility with the bacterium signifying the re-usability of the biohybrid. The biohybrid worked in ambient conditions (room temperature and pressure) with relatively low CO_2 concentrations ($\leq$20%). Also, the photocatalyst fabrication was made through the cheap and cost effective hot-injection synthesis without the need of any expensive vacuum processes.

While this study presents a proof-of-concept strategy for solar powered CO_2 to long chain chemical production, several opportunities exist for the overall optimisation of the process. With ethanol being a limiting component during fermentation with *C. kluyveri*, genomic engineering in *S. ovata* to favour ethanol production over acetate could improve the chain elongation efficiency in second step. Additionally, investigating symbiotic co-culturing of *S.* ovata and *C. kluyveri* could enable direct, one-pot conversion of CO_2 to fatty acids. Achieving such an integrated system, however, will require careful optimisation of metabolic flux coupling, light distribution, nutrient exchange, and temperature control to maintain balanced growth and coordinated activity between the two organisms. Another critical aspect is the reliance on sacrificial electron donors (SEDs). Replacing SEDs with valuable oxidative transformations (*e.g.*, glycerol or benzyl alcohol oxidation) could enhance overall efficiency and sustainability. Fabricating the biohybrid system into a configuration of large surface area

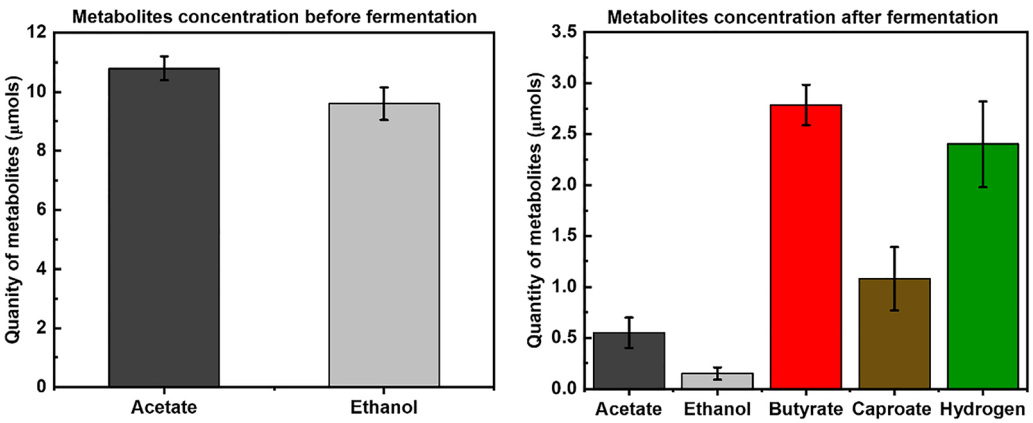

Fig. 10 Concentration profiles of metabolites during the fermentation process. Bar chart illustrating the bioconversion of acetate and ethanol into butyrate, caproate, and hydrogen over time, mediated by *C. kluyveri*. The data represent mean concentrations from three independent experiments. Error bars indicate standard deviation (s.d; n = 3).

sheet could yield to enhanced metabolite production as recent studies have successfully demonstrated.[77] Also, designing an automated flow system to separate the products could avoid product inhibition issues when using microbes, ultimately leading to overall improvement in the performance.

Experimental methods

CZTS nanoparticles synthesis

CZTS nanoparticles were synthesized using the commonly reported hot-injection method that involves the combination of metal precursors, sulfur in versatile nanoparticle synthesizing solvents like oleylamine. Initially, a solution of cation precursor was prepared in a composition with 1.32 mmol of copper(II) acetylacetonate, 0.79 mmol of zinc acetylacetonate hydrate, and 0.75 mmol of tin(IV) bis(acetylacetonate) dichloride in 50 mL oleyl amine. This solution was heated to 80 °C by maintaining the inert atmosphere condition. Simultaneously, 20 mL of 4.5 mmol sulfur in OLA was prepared and heated to 100 °C. The composition of the metal precursors and sulfur was selected to obtain a Cu-poor, Zn-rich composition in the CZTS nanoparticles.

The three-neck flask with cation precursors in oleyl amine was degassed for 15 min and purged with nitrogen, which is repeated twice. The flask was then subjected for vacuum heating until it reaches the boiling point and boiling continued again for 5 more min. The flask was then purged with nitrogen and the mixture temperature is heated up to 225 °C. The S-OLA solution which is being prepared parallelly was Injected into the cation precursor solution maintaining the reaction temperature at 225 °C for 30 min. After the product was allowed to cool down slowly to room temperature, it was mixed with toluene and Isopropanol (IPA) for 15 min and spined at 8500 rpm for 10 min. This centrifugation step was repeated multiple times to purify the sample and to initiate size profiling of the nanoparticles. To further refine the nanoparticle size distribution, the centrifuge speed was reduced to 7500 rpm for 3 minutes. At this speed, larger particles settled at the bottom while smaller nanoparticles remained suspended in the supernatant, allowing effective separation and control over the final CZTS nanoparticle size.

S. ovata culturing

The *S. ovata* strain was obtained from the DSMZ-German Collection of Microorganisms and Cell Cultures GmbH (DSM no. 2662). Cells were cultured in 100 mL serum vials using betaine as the electron donor, following the DSMZ-recommended growth medium, excluding casitone, sodium resazurin solution, and sodium sulfide (Table S3, SI). The medium was purged with a mixture of $N_2:CO_2$ (80 : 20) for 45 min prior to inoculation with the mother culture. After inoculation, the serum vials were incubated in a shaking incubator (Infors HT – Multitron Standard, 200 rpm, 303 K) for 5 days. The growth of *S. ovata* was monitored by measuring the OD_{600} of the culture at 2-day intervals.

C. kluyveri culturing

The *C. kluyveri* culture was purchased from DSMZ-German Collection of Microorganisms and Cell Cultures GmbH (DSM no. 555). The cells were cultured in 100 mL serum vials using ethanol and potassium acetate as the fermenting substrates, following the recommended growth medium but excluding sodium resazurin and sodium sulfide (Table S4, SI). The media was then purged with a mixture of $N_2:CO_2$ (80 : 20) for 45 min, after which 1 mL of the mother culture was inoculated. The serum vials containing the growing culture were incubated in a shaking incubator (Infors HT – Multitron Standard, 200 rpm, 303 K) for 10 days. The culture growth was monitored by measuring the OD_{600} at 4-day intervals.

Photocatalysis reaction

The photocatalysis reaction was conducted in a closed tubular photoreactor with side illumination from a Newport Oriel 67005 solar simulator (AM 1.5G, 100 mW cm^{-2}), calibrated using a certified Newport 1916-R optical power meter. A 100 mM TEOA solution was prepared in *S. ovat*a media (DSMZ 311) excluding betaine, Na-resazurin solution, casitone, L-cysteine, yeast extract, or Na_2S. The *S. ovata* culture was grown by incubating at 30 °C and 200 rpm for 5 days. After incubation, the culture was centrifuged at 4500 rpm for 5 min, washed three times with deionized (DI) water and fresh media. The resulting bacterial pellet was resuspended in the prepared TEOA solution, and the OD_{600} was adjusted to 1.0. The pH of the final suspension was adjusted to 7.3. This prepared solution was then added to the tubular photoreactor, which contained 10 mg of CZTS nanoparticles. The photoreactor was sealed with airtight rubber septa. Prior to light irradiation, the photoreactor was purged with a $N_2:CO_2$ gas mixture (80 : 20) for 45 min. The septa were further sealed with parafilm to ensure airtight conditions and prevent air contamination during the reaction

Chain elongation to fatty acids

Following five days of microbial photocatalysis, the contents of the reaction vial were filtered using a microfilter. In parallel, the *C. kluyveri* culture was harvested from incubation and washed three times with deionized water and fresh medium to remove residual components. The filtrate from the microbial photocatalysis products, containing acetate and ethanol, was then added to a falcon tube containing the washed *C. kluyveri* pellets. The mixture was vortexed thoroughly, and the final OD_{600} of the suspension was adjusted to 0.6. To establish an anoxic environment, the prepared suspension was transferred to a serum vial sealed with rubber caps and purged with an $N_2:CO_2$ (80 : 20) gas mixture for 45 minutes. The sealed vial was then incubated in a shaking incubator at 200 rpm and 37 °C to initiate fermentation.

Product quantification

The photosynthetic activity of the biohybrid system was monitored by quantifying the concentrations of CH_3COO^- and CH_3CH_2OH using quantitative ^1H NMR spectroscopy (Bruker

AvanceCore 400 MHz). TSP (3-(trimethylsilyl) propionic-2,2′,3,3′-d_4 acid sodium) in D_2O was used as the internal standard. Spectral data were processed using MestReNova software (version 15.0.1-35756). Quantification of the fermentation products was carried out by ^{1}H NMR spectroscopy, with signal integrals calibrated using external standards.

H_2 production from both biotic and abiotic systems was measured by direct injection into a Shimadzu GC-2010 Plus gas chromatograph, using a 1.0 mL Hamilton gas-tight syringe equipped with thermal conductivity detector operated at 250 °C. The chromatographic setup operates on an RT-Molsieve 5A column (30 m × 0.53 mm I.D., Restek), with argon as the carrier gas flows at a constant flow rate of 1 mL min^{-1}.

Raman spectroscopy

Raman microscopy of the samples was analysed using an Edinburgh Instruments RMS1000 – Multimodal Confocal Microscope. Various samples post photo experiment were probed to see the vibrational modes in both abiotic and biotic units of the biohybrid. The RMS 1000 system is equipped with high sensitivity CCD detector with narrow-band laser sources usually excited at 532 nm in 10–20% power range (5–10 mW). Special care was taken on optimising the laser power as excess power can damage the cells. The microscope was configured with 20× objective lens and 2 mm confocal resolution having 600 g mm^{-1}. The spectrometer acquired data from 0 to 3500 cm^{-1} in 5 accumulations with exposure time of 60 seconds. Measurements were taken at different locations for consistency. The reversibility in producing data suggests that the laser did not permanently damage the cells.

Confocal laser scanning microscopy (CLSM)

The biohybrids were stained with 3 μM SYTO 9 and 3 μM propidium iodide, then incubated in the dark for 20 minutes at 20 °C. Excitation wavelengths were λ_{ex} = 485 nm for SYTO 9 and λ_{ex} = 535 nm for PI, with emission wavelengths of λ_{em} = 495–530 nm for SYTO 9 and λ_{em} = 610–620 nm for PI.

CZTS characterisation

UV-Vis absorbance spectroscopy of the suspension of the CZTS was performed with PerkinElmer Lambda 1050+ UV/Vis/NIR spectrophotometer. SEM and elemental mapping (SEM–EDX) images were acquired using a TESCAN MIRA3 FEG-SEM equipped with an Oxford Instruments Aztec Energy X-maxN 150 system, operated at acceleration voltages of 5 kV and 20 kV, respectively. X-ray diffraction (XRD) measurements were performed using a Rigaku SmartLab SE diffractometer equipped with a D/teX Ultra 250 one-dimensional silicon strip detector and Cu Kα radiation (λ = 1.5418 Å) with Ni filters, operated at 40 kV and 50 mA in Bragg–Brentano geometry.

Selected area electron diffraction (SAED) patterns and high-resolution TEM (HRTEM) images were obtained using a JEOL 2100+ microscope. Scanning transmission electron microscopy (STEM) imaging and energy-dispersive X-ray spectroscopy (EDX) mapping were acquired using an aberration-corrected JEOL-NeoARM. Both instruments operated at an accelerating voltage of 200 kV. For data analysis, JEMS software was used to simulate electron diffraction patterns. Experimental SAED patterns were calibrated using a standard aluminium film as a reference.

The ICP–OES analysis of the CZTS were performed on an Agilent 5800 spectrometer. The samples underwent digestion in nitric acid (67–69%, trace metal analysis grade) for complete dissolution before ICP. Sulfur in CZTS was quantified using a Thermo Fisher Scientific FLASH 2000 CHNS/O analyser with V_2O_5 added to promote complete oxidation to SO_2. X-ray photoelectron spectroscopy (XPS) was conducted using a Kratos Axis Supra+ photoelectron spectrometer equipped with a monochromatized Al k-alpha source. For the high-resolution spectra, data were acquired using a pass energy of 20 eV and step size of 0.1 eV. Data analysis was performed using the IgorPro software with the XPST extension built in. The extraction of the valence and conduction-band values of the CZTS from the XPS/UPS measurements followed a standard procedure reported previously.[78]

Isotopic labelling experiments

The photobiocatalytic reaction over the CZTS–*S. ovata* biohybrid system were performed in a ^{13}C-labelled bicarbonate-buffered medium containing 47 mM Na$H^{13}CO_3$ (Sigma-Aldrich; 98 atom% ^{13}C, 99% CP). The reaction vials were purged with a pure N_2 for 30 min followed by $^{13}CO_2$ gas (CK Isotopes; ^{13}C, 99% CP, <1% ^{18}O) to establish the headspace atmosphere under otherwise identical conditions to the standard experiments. Aliquots were collected after 5 days illumination, and the formation of ^{13}C-labelled acetate was quantified by ^{1}H NMR spectroscopy using a Bruker 400 MHz spectrometer. Spectral assignments confirming $^{13}CH_3{}^{13}COO^-$ formation are provided in the SI (Fig. S13).

Photoelectrochemical characterization of the CZTS

CZTS films were fabricated on a Mo-coated glass substrate by slot-die coating nanoparticle inks dissolved in hexanethiol. After annealing at 300 °C for 5 min over open hotplate (soft baking process), the conductive Mo layer was made in contact with a Ti rod, soldered with Cu tap and parafilm. The photoelectrochemical characterization of the films was done over a three-electrode configuration with Ag/AgCl as reference electrode and Pt as counter electrode respectively. A 0.5 M K_2SO_4 solution was used as the electrolyte. For the chronoamperometric measurements, −0.25 V (v/s Ag/AgCl) was applied over the working electrode in light on/off condition in 50 mV intervals. Prior to irradiation using a 300 W Xe lamp, the reactor was thoroughly purged with nitrogen to remove both the headspace and dissolved oxygen in the electrolyte.

Zeta potential measurements

Zeta potential measurement of the CZTS nanoparticles was performed over a Malvern Zetasizer Nano at 25 °C. Samples (0.1 mg mL^{-1} in Milli-Q water) after 30 min of sonication were filtered (0.22 μm) and equilibrated for 2 min before measurement. Zeta potential measurements of *S. ovata* cells were performed with the same procedure, excluding the sonication and filtration steps. Zeta potential was determined *via* laser Doppler

electrophoresis using a DTS1070 capillary zeta cell, applying the Smoluchowski model.

Statistics and reproducibility

Mean values and standard deviation were calculated using the averageif and StdDev functions in OriginPro. For SEM (and EDX composition and mapping), 2–3 distinct regions with similar morphologies were captured per specimen. Representative images are shown.

Author contributions

M. Rishan, S. Kalathil and E. A. Gibson, G. Zoppi conceived the idea and designed the project. M. Rishan carried out the experiments and wrote the manuscript. M. Rishan and P. Punathil synthesized the CZTS nanoparticles. E. Arca performed the XPS analysis of the CZTS nanoparticles. C. Burns carried out the Raman analysis of the biohybrid. J. C. A Do Nascimento and V. Lazarov performed the TEM study of the CZTS nanoparticles. S. Kalathil, E. A. Gibson and M. Hayes supervised the project and edited the manuscript. S. Kalathil, E. A. Gibson, M. Hayes and G. Zoppi acquired the funding for the project.

Conflicts of interest

There are no conflicts to declare.

Data availability

All experimental data supporting this study are available within the article and its supplementary information (SI). Additional raw datasets and protocols can be obtained from the corresponding author upon reasonable request. Supplementary information is available. See DOI: https://doi.org/10.1039/d5mh02330k.

Acknowledgements

This work was supported by the EPSRC Centre for Doctoral Training in Renewable Energy Northeast Universities (ReNU) (EP/S023836/1), Reimagining Photovoltaics Manufacturing (EP/W010062/1) and Johnson Matthey in collaboration with researchers at Northumbria University, Newcastle, UK and Newcastle University, Newcastle, UK. E. A. acknowledges support by the Engineering and Physical Sciences Research Council (EP/X032116/1). XPS/UPS data was acquired at the EPSRC National Facility for XPS (HarwellXPS, EP/Y023587/1, EP/Y023609/1, EP/Y023536/1, EP/Y023552/1 and EP/Y023544/1).

References

1 A. Goeppert, M. Czaun, G. S. Prakash and G. A. Olah, *Energy Environ. Sci.*, 2012, **5**, 7833–7853.
2 N. S. Lewis, *Science*, 2016, **351**, aad1920.
3 C. Jiang, S. J. Moniz, A. Wang, T. Zhang and J. Tang, *Chem. Soc. Rev.*, 2017, **46**, 4645–4660.
4 X. Chen, S. Shen, L. Guo and S. S. Mao, *Chem. Rev.*, 2010, **110**, 6503–6570.
5 J. Barber, *Chem. Soc. Rev.*, 2009, **38**, 185–196.
6 F. Wen and C. Li, *Acc. Chem. Res.*, 2013, **46**, 2355–2364.
7 S. Xie, Q. Zhang, G. Liu and Y. Wang, *Chem. Commun.*, 2016, **52**, 35–59.
8 S. Yoshino, T. Takayama, Y. Yamaguchi, A. Iwase and A. Kudo, *Acc. Chem. Res.*, 2022, **55**, 966–977.
9 D. G. Nocera, *Acc. Chem. Res.*, 2017, **50**, 616–619.
10 S. A. Younis and K.-H. Kim, *Catalysts*, 2020, **10**, 1109.
11 N. Kornienko, J. Z. Zhang, K. K. Sakimoto, P. Yang and E. Reisner, *Nat. Nanotechnol.*, 2018, **13**, 890–899.
12 X. Fang, S. Kalathil and E. Reisner, *Chem. Soc. Rev.*, 2020, **49**, 4926–4952.
13 N. Plumeré, O. Rüdiger, A. A. Oughli, R. Williams, J. Vivekananthan, S. Pöller, W. Schuhmann and W. Lubitz, *Nat. Chem.*, 2014, **6**, 822–827.
14 S. Cestellos-Blanco, H. Zhang, J. M. Kim, Y.-X. Shen and P. Yang, *Nat. Catal.*, 2020, **3**, 245–255.
15 Z. Liu, K. Wang, Y. Chen, T. Tan and J. Nielsen, *Nat. Catal.*, 2020, **3**, 274–288.
16 J. Madjarov, R. Soares, C. M. Paquete and R. O. Louro, *Front. Microbiol.*, 2022, **13**, 913311.
17 W. Yu, M. V. Pavliuk, A. Liu, Y. Zeng, S. Xia, Y. Huang, H. Bai, F. Lv, H. Tian and S. Wang, *ACS Appl. Mater. Interfaces*, 2022, **15**, 2183–2191.
18 P. Gai, W. Yu, H. Zhao, R. Qi, F. Li, L. Liu, F. Lv and S. Wang, *Angew. Chem., Int. Ed.*, 2020, **59**, 7224–7229.
19 Y. Honda, H. Hagiwara, S. Ida and T. Ishihara, *Angew. Chem.*, 2016, **128**, 8177–8180.
20 W. Wei, P. Sun, Z. Li, K. Song, W. Su, B. Wang, Y. Liu and J. Zhao, *Sci. Adv.*, 2018, **4**, eaap9253.
21 K. Gurunathan, *J. Mol. Catal. A: Chem.*, 2000, **156**, 59–67.
22 K. K. Sakimoto, A. B. Wong and P. Yang, *Science*, 2016, **351**, 74–77.
23 J. Trevors, G. Stratton and G. Gadd, *Can. J. Microbiol.*, 1986, **32**, 447–464.
24 Y. Qu, G. Zoppi and N. S. Beattie, *Prog. Photovoltaics Res. Appl.*, 2016, **24**, 836–845.
25 C. K. Miskin, W. C. Yang, C. J. Hages, N. J. Carter, C. S. Joglekar, E. A. Stach and R. Agrawal, *Prog. Photovoltaics Res. Appl.*, 2015, **23**, 654–659.
26 J. Z. Zhang, *Acc. Chem. Res.*, 1997, **30**, 423–429.
27 Q. Guo, H. W. Hillhouse and R. Agrawal, *J. Am. Chem. Soc.*, 2009, **131**, 11672–11673.
28 S. M. Camara, L. Wang and X. Zhang, *Nanotechnology*, 2013, **24**, 495401.
29 S. Ahmadi, N. Khemiri, A. Cantarero and M. Kanzari, *J. Alloys Compd.*, 2022, **925**, 166520.
30 B.-T. Jheng, P.-T. Liu and M.-C. Wu, *Sol. Energy Mater. Sol. Cells*, 2014, **128**, 275–282.
31 H. Jiang, P. Dai, Z. Feng, W. Fan and J. Zhan, *J. Mater. Chem.*, 2012, **22**, 7502–7506.
32 A. Singh, H. Geaney, F. Laffir and K. M. Ryan, *J. Am. Chem. Soc.*, 2012, **134**, 2910–2913.

33 X. Yin, C. Tang, M. Chen, S. Adams, H. Wang and H. Gong, *J. Mater. Chem. A*, 2013, **1**, 7927–7932.
34 P. Dai, X. Shen, Z. Lin, Z. Feng, H. Xu and J. Zhan, *Chem. Commun.*, 2010, **46**, 5749–5751.
35 X. Wang, Y. Ruan, S. Feng, S. Chen and K. Su, *ACS Sustainable Chem. Eng.*, 2018, **6**, 11424–11432.
36 K. Kim, A. Razzaq, S. Sorcar, Y. Park, C. A. Grimes and S.-I. In, *RSC Adv.*, 2016, **6**, 38964–38971.
37 E. Ha, L. Lee, J. Wang, F. Li, K.-Y. Wong and S. Tsang, *Adv. Mater.*, 2014, **26**, 3496–3500.
38 X. Yu, X. An, A. Genc, M. Ibanez, J. Arbiol, Y. Zhang and A. Cabot, *J. Phys. Chem. C*, 2015, **119**, 21882–21888.
39 X. Yu, A. Shavel, X. An, Z. Luo, M. Ibáñez and A. Cabot, *J. Am. Chem. Soc.*, 2014, **136**, 9236–9239.
40 Y. Ding, J. R. Bertram, C. Eckert, R. R. Bommareddy, R. Patel, A. Conradie, S. Bryan and P. Nagpal, *J. Am. Chem. Soc.*, 2019, **141**, 10272–10282.
41 E. Blanchet, F. Duquenne, Y. Rafrafi, L. Etcheverry, B. Erable and A. Bergel, *Energy Environ. Sci.*, 2015, **8**, 3731–3744.
42 K. P. Nevin, T. L. Woodard, A. E. Franks, Z. M. Summers and D. R. Lovley, *mBio*, 2010, **1**(2), e00103–10.
43 G. V. Last and M. T. Schmick, *Environ. Earth Sci.*, 2015, **74**, 1189–1198.
44 R. A. Frimpong, H. Nikolic, D. Bahr, G. Kiran and K. Liu, *Int. J. Greenhouse Gas Control*, 2021, **106**, 103290.
45 Y. He, S. Wang, X. Han, J. Shen, Y. Lu, J. Zhao, C. Shen and L. Qiao, *ACS Appl. Mater. Interfaces*, 2022, **14**, 23364–23374.
46 Q. Wang, S. Kalathil, C. Pornrungroj, C. D. Sahm and E. Reisner, *Nat. Catal.*, 2022, **5**, 633–641.
47 H. L. Drake, A. S. Gößner and S. L. Daniel, *Ann. N. Y. Acad. Sci.*, 2008, **1125**, 100–128.
48 A. J. Grethlein and M. K. Jain, *Trends Biotechnol.*, 1992, **10**, 418–423.
49 S. W. Ragsdale and E. Pierce, *Biochim. Biophys. Acta, Proteins Proteomics*, 2008, **1784**, 1873–1898.
50 B. Möller, R. Oßmer, B. H. Howard, G. Gottschalk and H. Hippe, *Arch. Microbiol.*, 1984, **139**, 388–396.
51 M. Visser, M. M. Pieterse, M. W. Pinkse, B. Nijsse, P. D. Verhaert, W. M. de Vos, P. J. Schaap and A. J. Stams, *Environ. Microbiol.*, 2016, **18**, 2843–2855.
52 K. Schuchmann and V. Müller, *Appl. Environ. Microbiol.*, 2016, **82**, 4056–4069.
53 P.-L. Tremblay and T. Zhang, *Appl. Environ. Microbiol.*, 2024, **90**, e0175723.
54 J. Bertsch and V. Müller, *Biotechnol. Biofuels*, 2015, **8**, 1–12.
55 F. Ammam, P.-L. Tremblay, D. M. Lizak and T. Zhang, *Biotechnol. Biofuels*, 2016, **9**, 1–10.
56 P.-L. Tremblay, D. Höglund, A. Koza, I. Bonde and T. Zhang, *Sci. Rep.*, 2015, **5**, 16168.
57 S. Chu, W. Li, Y. Yan, T. Hamann, I. Shih, D. Wang and Z. Mi, *Nano Futures*, 2017, **1**, 022001.
58 I. L. B. Robertson, H. Zhang, E. Reisner, J. N. Butt and L. J. Jeuken, *Chem. Sci.*, 2024, **15**, 9893–9914.
59 Y. Qu, G. Zoppi, R. W. Miles and N. S. Beattie, *Mater. Res. Express*, 2014, **1**, 045040.
60 M. Altosaar, J. Raudoja, K. Timmo, M. Danilson, M. Grossberg, J. Krustok and E. Mellikov, *Phys. Status Solidi A*, 2008, **205**, 167–170.
61 Z. Chen, H. Zhang, P. Guo, J. Zhang, G. Tira, Y. J. Kim, Y. A. Wu, Y. Liu, J. Wen and T. Rajh, *J. Am. Chem. Soc.*, 2019, **141**, 11811–11815.
62 K. Zhang, R. Li, J. Chen, L. Chai, Z. Lin, L. Zou and Y. Shi, *Appl. Catal., B*, 2024, **342**, 123375.
63 T. J. Beveridge and L. L. Graham, *Microbiol. Rev.*, 1991, **55**, 684–705.
64 P. Millard, J.-C. Portais and P. Mendes, *BMC Syst. Biol.*, 2015, **9**, 64.
65 T. M. Wasylenko and G. Stephanopoulos, *Biotechnol. J.*, 2013, **8**, 1080–1089.
66 K. Schuchmann and V. Müller, *Nat. Rev. Microbiol.*, 2014, **12**, 809–821.
67 Y. Kim, S. Lama, D. Agrawal, V. Kumar and S. Park, *Biotechnol. Adv.*, 2021, **49**, 107736.
68 H. Huang, *Plastics from Bacteria: Natural Functions and Applications*, 2010, pp, 389–404.
69 D. Kiefer, M. Merkel, L. Lilge, M. Henkel and R. Hausmann, *Trends Biotechnol.*, 2021, **39**, 397–411.
70 H. Barker, M. Kamen and B. Bornstein, *Proc. Natl. Acad. Sci. U. S. A.*, 1945, **31**, 373–381.
71 B. G. Harvey and H. A. Meylemans, *Green Chem.*, 2014, **16**, 770–776.
72 M. Dwidar, J.-Y. Park, R. J. Mitchell and B.-I. Sang, *Sci. World J.*, 2012, **2012**, 471417.
73 C. M. Spirito, H. Richter, K. Rabaey, A. J. Stams and L. T. Angenent, *Curr. Opin. Biotechnol*, 2014, **27**, 115–122.
74 M. V. Reddy, S. V. Mohan and Y.-C. Chang, *Appl. Biochem. Biotechnol.*, 2018, **185**, 594–605.
75 L. A. Kucek, M. Nguyen and L. T. Angenent, *Water Res.*, 2016, **93**, 163–171.
76 R. Thauer, K. Jungermann, H. Henninger, J. Wenning and K. Decker, *Eur. J. Biochem.*, 1968, **4**, 173–180.
77 N. Wen, Q. Jiang and D. Liu, *Sci. Adv.*, 2024, **10**, eadp8567.
78 T. D. Veal, D. O. Scanlon, R. Kostecki and E. Arca, *J. Phys.: Energy*, 2021, **3**, 032001.